IEEE Sensors Council
IEEE SENSORS JOURNAL, VOL. 24, NO. 5, 1 MARCH 2024

High-Resolved Near-Field Sensing by Means of Dielectric Grating With a Box-Like Resonance Shape

Annarita di Toma, Giuseppe Brunetti, Paola Colapietro, and Caterina Ciminelli, *Senior Member, IEEE*

***Abstract*—In the last ten years, advances in diagnosis and treatment have played a significant role in counteracting the growth of dangerous diseases. Recently, several studies have demonstrated that monitoring proteins in the human body helps predictive monitoring of human health conditions and disease progress. In this context, bio-recognition techniques with high resolution are crucial. Evanescent-field biosensors have been widely investigated and successfully developed thanks to their ultrahigh sensitivity. However, their resolution is mitigated by the nature of the Lorentzian spectral line shape that shows inevitable significant spectral overlap among similar concentration-related resonances. To overcome this problem, a novel ultra-compact photonic biosensor with a tailored resonance shape is proposed. The device consists of 1-D photonic crystal (PhC) with engineered defects to achieve resonance with a box-like shape, a very large roll-off (=−10.50 dB/oct.), within a small footprint (≈$1 \cdot 10^{-2}$ μm^2), enabling single wavelength interrogation. The strong biosensor–analyte interaction is associated with a larger transmission change with respect to biosensors with Lorentzian shape (>4 versus >0.5 dB for proteins Immunoglobulin-G (IgG) concentration from 1 to 500 pg/mL), drastically decreasing the read errors.**

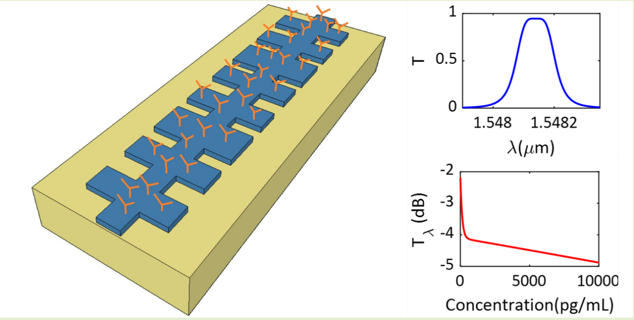

***Index Terms*—Biosensors, lab-on-a-chip (LOC), photonic crystals (PhCs), sensor modeling, silicon photonics.**

I. Introduction

PROTEINS are involved in several processes throughout the human body, including transporting substances, storing nutrients, and speeding up chemical processes [1]. Monitoring proteins helps in understanding human health conditions and disease progress [1]. During the last few years, a great research effort has been spent to map human proteins in cells, tissues, organs, and blood, using the integration of different technologies, including antibody-based imaging, mass spectrometry-based proteomics, transcriptomics, proximity extension assay-based protein profiling, and systems biology. In this framework, integrated optical biosensors are becoming one of the most promising technologies to detect biomolecules, viruses, bacteria, and bio-analytes, guaranteeing highly sensitive, versatile, portable, and easy-to-use point-of-care (POC) devices that could have a great impact on health care and environmental fields [8]. Integrated optical biosensors support the development of systems, called lab-on-a-chip (LOC), able to perform real-time-multiplexed recognition, also preserving the system's stability [2], [3], [4].

Optical label-free LOCs are mainly based on evanescent field sensing, according to which the evanescent electric field tails can detect changes in refractive index at the cladding/core interface. In this way, any perturbation of the field in the cladding area leads to an effective refractive index change of the guided mode [5], [6]. Hence, the sensitivity of evanescent wave biosensors is strictly correlated to the interaction between the target analytes and the evanescent field. Starting from conventional photonic wires [7], the performance of simple waveguide-based devices, such as the ring resonators, is affected by the large confinement of the mode within the core or cladding for transverse electric (TE) and transverse magnetic (TM) mode, respectively. A sensitivity of 361.3 nm/RIU with a Q-factor of 1143 has been proposed in [8] for a whispering gallery mode (WGM) ring resonator. To maximize the overlapping between the field and the analytes, innovative architectures have been proposed in the literature. In particular, promising results have been achieved using sub-wavelength gratings (SWGs), able to tailor

---

Manuscript received 22 December 2023; accepted 2 January 2024. Date of publication 12 January 2024; date of current version 29 February 2024. The associate editor coordinating the review of this article and approving it for publication was Dr. Daniele Tosi. *(Corresponding author: Caterina Ciminelli.)*

The authors are with the Optoelectronics Laboratory, Department of Electrical and Information Engineering, Politecnico di Bari, 70126 Bari, Italy (e-mail: a.ditoma@phd.poliba.it; giuseppe.brunetti@poliba.it; p.colapietro@phd.poliba.it; caterina.ciminelli@poliba.it).

Digital Object Identifier 10.1109/JSEN.2024.3349948

the spatial distribution of the mode profile. A high sensitivity (605 nm/RIU) with a limit of detection (LOD) of $1.30 \cdot 10^{-4}$ RIU has been obtained (RIU: Refractive Index Unit) [9]. The high sensitivity collides with the large vulnerability and damageability during and after the fabrication which limits their suitability for portable sensing [10]. To overcome this limit and exploit the resonant behavior, ring resonator sensors with SWG waveguides consisting of a "fishbone" structure have been proposed to solve this downside [11]. Bulk sensitivities up to 349 and 438 nm/RIU have been achieved at 1310 and 1550 nm, respectively, and intrinsic LODs as low as $5.1 \cdot 10^{-4}$ and $7.1 \cdot 10^{-4}$ RIU [11]. The main limits of this solution are linked to the complex architecture, the small coupling region, and the wider footprint with respect to a single rib waveguide.

In the context of evanescent field sensing, remarkable performance has been achieved using BiModal Waveguide (BiMW) interferometers, based on the interference between TE and TM modes within the waveguide, that enhance the interaction mode analyte, providing higher sensitivity (=1350 nm/RIU [12]), lower LOD ($=2 \cdot 10^{-5}$ RIU [12]), reliability, and robustness within a compact footprint [13]. The BiMW interferometer sensitivity has been further improved by carrying the benefits mentioned above of SWGs or photonic crystals (PhCs) [12], [14], at the expense of a larger footprint [3] and complex excitation of both modes with the same amplitude which is crucial to reach the phase matching condition [3]. The latter affects the modulation depth, making complex the detection of the resonant peak.

Another widely investigated common-path interferometric sensor is based on guided-mode resonance (GMR). It exploits the simultaneous excitation of two orthogonally polarized modes to detect the relative phase change due to the presence of a biomolecule on the sensor surface [15]. The readout is based on the Fourier transform technique. A sensitivity of 289 π/RIU with a LOD of about 1.8×10^{-6} RIU has been proposed in [16]. However, environmental noise could strictly affect the LOD [16].

Finally, although the aforementioned sensors show promising values of both sensitivity and LOD, their use in LOC is limited by their Lorentzian spectrum. In LOC, the excitation is commonly performed using a single-wavelength laser and the readout aims at detecting the intensity changes due to the shift of the wavelength related to concentration variation [17].

However, when a single wavelength source is used for the waveguide excitation of a Lorentzian shape sensor, small concentration shifts lead to undetectable transmission change, resulting in large crosstalk and, in turn, detection mistakes. This issue is correlated to the very slow roll-off, expressed as the change of the transmission over the resonance edges, of Lorentzian-shape resonances (of the order of a few a.u./nm). To solve this huge problem and obtain high sensitivity with low LOD, here, we propose a silicon biosensor, based on an engineered sidewall grating to achieve a high-Q box-like resonance shape, characterized by a large Q-factor $>10^4$, Extinction Ratio (ER) >15 dB, flat band, and a rapid roll-off (>-10.50 dB/oct.). Moreover, to our knowledge, the proposed biosensor shows a very high bulk sensitivity (=490.49 nm/RIU), one of the highest achieved by resonant devices, together with the advantages of a small footprint and a simple fabrication process, also guaranteeing to distinguish similar concentration values. The performance is suitable for high-resolvable sensing using a simple architecture with a single-wavelength laser, aiming at detecting, at a single wavelength, the transmission variation when the concentration changes. A large and noticeable change in the resonance transmission (more than 4 dB) by varying the protein concentration from 1 up to 500 pg/mL has been achieved. The detection has been simulated considering Immunoglobulin G (IgG) as the target protein and anti-IgG antibodies immobilized on the surface of the sensor [18]. IgG is a glycoprotein produced by the immune system in response to the presence of foreign substances called antigens, such as bacteria, viruses, or other pathogens. IgG is the most abundant antibody in the human body, accounting for approximately 75%–80% of all antibodies present in the bloodstream. While traditionally recognized for its role in fighting infections by recognizing and neutralizing pathogens, there is emerging research suggesting that changes in IgG levels or specific IgG antibodies may have implications in cancer prediction, diagnosis, and monitoring. It is important to note that the device could be employed for sensing other types of proteins by merely altering the antibody while maintaining the same sensitivity.

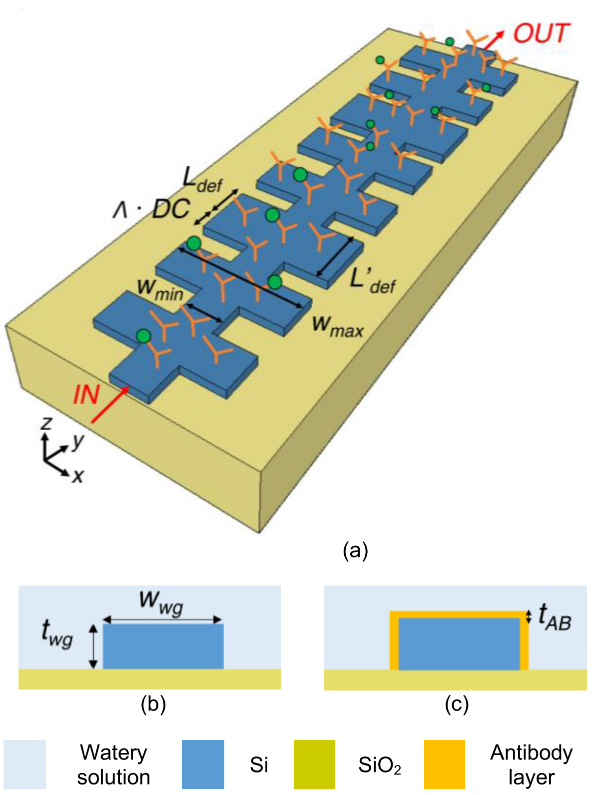

(a)

(b) (c)

Fig. 1. (a) Sidewall grating waveguide with deposited antibodies (labeled as orange Ys) and target analytes (green dots). Cross section of the rib waveguide (b) without antibody layer and (c) with deposited antibody layer.

II. PROPOSED DEVICE

The proposed device consists of a sidewall grating in silicon-on-insulator (SOI) technology [Fig. 1(a)], with a modulation of the width, that ranges from a maximum value

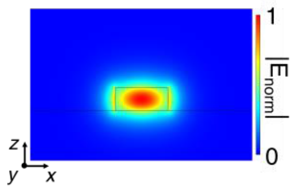

(a) (b)

Fig. 2. Electric field distribution of (a) TE ($n_{\mathrm{eff}} = 2.42883$) and (b) TM ($n_{\mathrm{eff}} = 1.70525$) modes at 1550 nm, achieved by COMSOL Multiphysics FEM simulations.

($w_{\max}$) to a minimum one ($w_{\min}$), with a duty-cycle dc, of the bare waveguide. The grating shows N_t grating semi-periods, 1-D arranged with a period Λ, and length dc $\times$ Λ. The unfunctionalized device cross section is depicted in Fig. 1(b), with a thickness t_{wg} and a width w_{wg} of 220 and 450 nm, respectively.

The widths $w_{\max}$ and $w_{\min}$ have been engineered using a finite element method (FEM)-based solver (COMSOL Multiphysics[1]), aiming at preserving the mono-modality and avoiding a strong increase in the losses.

A $w_{\max} = 500$ nm has been designed to avoid extra-order mode excitation. Moreover, since the propagation losses can be considered fixed within the range $w_{wg} \pm 80$ nm, according to [24], a waveguide modulation $\Delta w = w_{\max} - w_{wg} = w_{wg} - w_{\min} = 50$ nm, with $w_{\mathrm{wax}} = 500$ nm and $w_{\mathrm{win}} = 400$ nm, has been considered, preserving the uniformity of the losses along the whole device.

In the comparison between Fig. 2(a) and (b), the TM$_0$ mode shows lower confinement within the core with respect to the TE$_0$ mode, with a resulting more intense interaction at the solution-silicon interface. Moreover, since the TM$_0$ mode interacts more with the vertical surfaces than the rough sidewall ones, the TM$_0$ propagation losses are lower than the TE$_0$ ones [19]. Moreover, by considering the effective refractive index of both grating sections, a period $\Lambda = 465$ nm and dc $= 50$ % have been chosen, to ensure the operation at $\approx$1550 nm.

The insertion of defects, L_{def} long and $w_{\max}$ wide, placed in cascade to $w_{\max}$ wide and $\Lambda \times$ dc long semi-periods within the sidewall grating architecture, as shown in Fig. 1(a), allows tailoring the resonance toward a box-like shape starting from a Lorentzian-one. The insertion of multiple defects into the grating causes the formation of coupled Fabry–Perot (FP) resonant cavities. Light can propagate into the grating from one cavity to the next one, resulting in a transmission spectrum with as many ripples in the resonance as the number of defects. This behavior is linked to the interactions between the evanescent cavity modes. The defect and the overall length L_{def} and L'_{def}, respectively, have been designed to achieve a phase shift of $\pi/2$ at the Bragg wavelength [25], as

$$L_{\mathrm{def}} = \frac{4m+1}{4}\frac{\lambda_B}{n_{\mathrm{eff-def}}} \qquad m = 1, 2, \ldots \tag{1}$$

$$L'_{\mathrm{def}} = \mathrm{dc} \cdot \Lambda + L_{\mathrm{def}} \tag{2}$$

where λ_B is the Bragg wavelength ($\approx$1550 nm), m represents the grating order, and $n_{\mathrm{eff-def}}$ is the effective refractive index of the defect region (=1.66381 at 1550 nm).

TABLE I

PERFORMANCE COMPARISON BY VARYING M, N_t, AND N_{def}

m	N_t	N_{def}	Q-factor	ER (dB)	CR (%)	Roll-off (dB/oct.)
5	128	2	541	27.79	74.71	7.66
10	128	2	1,218	34.96	74.80	10.84
50	128	2	2,981	29.32	74.62	7.72
100	128	2	11,994	15.35	74.06	10.50
150	128	2	8,334	31.01	74.18	8.14
100	32	2	707	8.71	73.92	5.66
100	64	2	1,144	21.15	74.38	10.14
100	128	2	11,994	15.35	74.06	10.50
100	256	2	128,531	5.49	63.48	7.13
100	128	1	77,386	31.76	57.23	4.01
100	128	2	11,994	15.35	74.06	10.50
100	128	3	3,398	25.07	63.95	8.07
100	128	4	2,203	24.28	74.96	12.18
100	128	5	1,659	27.55	73.02	12.23

To simulate the transmission spectra of the proposed biosensors, a self-made mathematical model has been used, based on both the effective index method [26] and the 2D-Transmission Matrix Method (TMM) [27], where each semi-period/defect has been studied through the related S-parameters, that take into account the transmission and reflection of the waves at the related input–output interfaces. The TMM allows representing the system as a network of interconnected elements, where each element's response is characterized by a transmission matrix. These matrices describe how light interacts with each component, incorporating factors like reflection, transmission, and phase shifts. By cascading these matrices together, the method allows for the efficient analysis of complex optical systems. In particular, it enables predicting propagation, transmission, and reflection of the light within the system without the need for solving the entire system simultaneously. Specifically, the transfer matrices of the input section, the output section, the defect region, the $w_{\min}$-, and the $w_{\max}$-wide sections have been cascaded and multiplied according to the design of the structure.

As commonly performed in literature [28], [29], overestimated propagation losses of about 1 dB/cm have been considered. This value considers any loss, caused by grating reflections, evanescent fields, surface roughness, and any mismatch between nominal and fabricated features.

Assuming the position of the defects within the grating as Newton's binomial series [25], a distribution of resonances centered at the Bragg wavelength with a resulting flat-band box-like envelope is expected. All the grating features, such as m, the number of defects N_{def}, and the total number of grating semi-periods N_t, which should be a power of 2 to satisfy Newton's role, have been engineered through iterative simulations, aiming at simultaneously enhancing roll-off, ER, and Q-factor. To rate the box-like-behavior, the coincidence ratio (CR), expressed as the ratio between the area under the curve limited at the full-width-at-half-maximum (FWHM) values and the box one with the same amplitude, has been evaluated. CR values larger than 70% represent a good approximation of a box-like shape [30]. Table I summarizes all the grating performance, in terms of Q-factor, ER, CR, and roll-off.

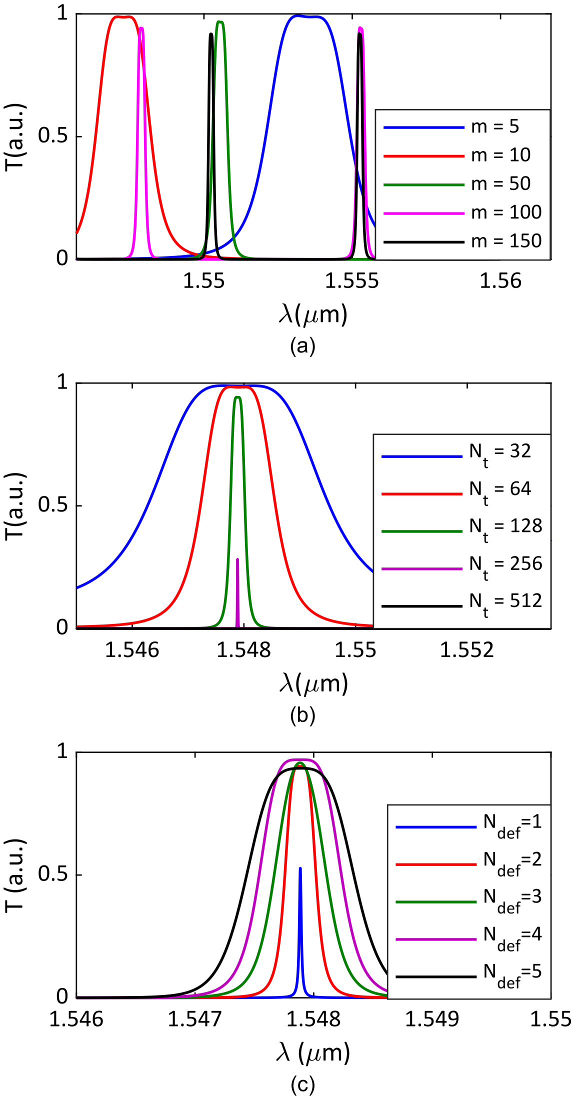

(a)

(b)

(c)

Fig. 3. Transmission spectra of the waveguide by varying (a) m ($N_t = 128$, $N_{\text{def}} = 2$), (b) N_t ($m = 100$, $N_{\text{def}} = 2$), and (c) N_{def} ($m = 100$, $N_t = 128$).

As initial conditions of the design, a value of $N_t = 128$ and $N_{\text{def}} = 2$ have been considered. Fig. 3(a) represents the spectra behavior by varying m. It is possible to observe that the increase of m leads to an increase in the Q-factor and roll-off, a decrease in the ER, and a random shift of the resonance, at the expense of a larger footprint. As m increases the length of the established FP cavities increases, which causes both a larger Q-factor and roll-off, and lower ER, as the typical FP behavior, although preserving the box-like shape (as highlighted by CR values in Table I). Although m increase is associated with an improvement of Q-factor and roll-off, a value of $m = 100$ ($L'_{\text{def}} = 91$ μm) has been considered aiming at achieving a Q-factor of 1.2×10^4, also preserving the device compactness and the box-like shape. About the random resonance shift, this effect is due to the rounding down or up of the L_{def} value, according to (1), that causes a blue- or red-shift of the resonance, respectively.

By varying N_t [see Fig. 3(b)], the resonance shows an increase of the Q-factor and the roll-off at the expense of a dramatic decrease in the ER. An increase of N_t leads to an enlargement of FP mirrors, with a resulting increase of Q-factor according to the FP theory [31]. However, an increase in the grating length involves an increase in losses, that strongly counteracts the Q-factor increase, with a resulting resonance envelope that loses the box-like shape, as confirmed by the CR values in Table I. A value $N_t = 128$ represents the best compromise to achieve a high Q-factor, and a large ER, also preserving the box-like shape.

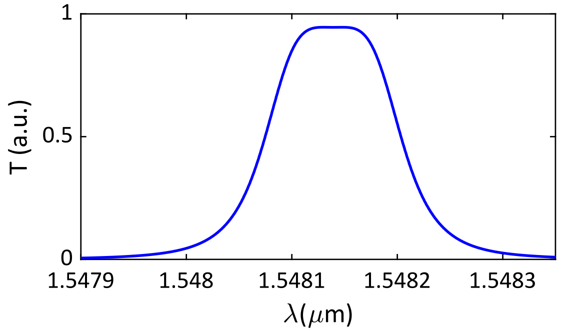

Fig. 4. Transmission spectra of the designed grating with $N_t = 128$, $N_{\text{def}} = 2$, $m = 100$ ($L_{\text{def}} = 91$ μm), and a total length of 212 μm.

The change of N_{def}, represented in Fig. 3(c), is associated with a stronger tailoring of the resonance toward a box-like shape, at the expense of a lower Q-factor although with an increase of ER. This effect is more evident for an even number of defects. The different behavior between odd and even defects is related to the coefficients of Newton's role. An even number of defects establishes a symmetric structure, e.g., for $N_{\text{def}} = 2$ and $N_t = 128$, the grating is made of the sequence: 32 semiperiods − 1 defect − 64 semiperiods − 1 defect − 32 semiperiods. The multiple FP cavities generate two identical and symmetrical resonances with respect to the Bragg wavelength, with a resulting quasi-flat top band of the envelope. Indeed, as an example, for $N_{\text{def}} = 3$ and $N_t = 128$, the grating consists of the sequence: 16 semiperiods − 1 defect − 48 semiperiods − 1 defect − 48 semiperiods − 1 defect − 16 semiperiods, resulting asymmetric. Therefore, the generated resonances are not identical to an overall envelope that shows a lower CR value with respect to the even defects-based grating.

In the final analysis, as arises in Table I, the roll-off tends to increase as both the ER and Q-factor increase. A higher Q-factor, which results in better selectivity, often leads to a sharper transition between the passband and stopband, potentially causing a faster roll-off at the edges of the filter's response. Similarly, an increased ER, highlighting the contrast between signal states, can also contribute to a steeper transition in the filter, making it more sensitive to variations in signal levels and consequently amplifying the roll-off effect.

Finally, a grating with $N_t = 128$, $N_{\text{def}} = 2$, $m = 100$ with a total length of 212 μm is the best compromise, guarantying a Q-factor $= 1.2 \times 10^4$, ER $= 15.35$ dB, roll-off $= -10.50$ dB/oct., and box-like CR $= 74.06\%$ (see Fig. 4).

III. BIOSENSOR PERFORMANCE

Aiming at detecting the concentration of proteins diluted within a watery solution, an anti-IgG layer is deposited over

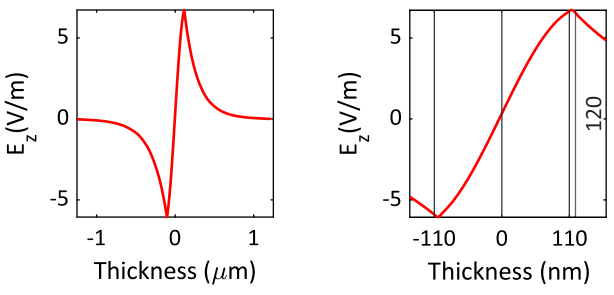

(a)

(b)

Fig. 5. (a) TM mode electric field z-component versus waveguide thickness. (b) Zoomed-in view the core region. The position "0" is set in the middle of the waveguide core.

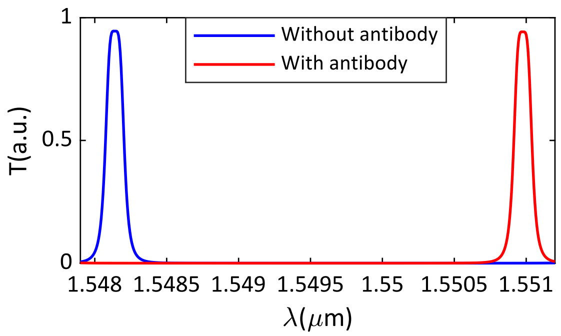

Fig. 6. Spectrum of the designed grating before (blue curve) and after (red curve) deposition of antibody layer.

the whole top surface of the grating. According to the literature [18], a layer with thickness $t_{AB} = 10$ nm and a refractive index of 1.45 has been considered, as SiO_2, to mimic the features of a typical binding of IgG and anti-IgG layer. The variation of the IgG concentration affects the layer refractive index, leaving unaltered the layer thickness since the designed antibody layer takes already into account the IgG − anti-IgG bounding distance, as demonstrated in [18] and [31]. As shown in Fig. 5, the electric field confinement within the layer 10 nm guarantees a large sensor sensitivity. In particular, the evanescent field is very large (≈98%), where the link between antibody and target IgG occurs (range of thickness 110–120 nm).

Although the proposed sensor has been designed for a single-wavelength interrogation system, whose operation is based on the detection of amplitude change at a single-wavelength, the resonance shift $\delta\lambda_{\mathrm{RES}}$ has been evaluated to rate the most common sensor performance, in terms of bulk/surface sensitivity. Even if Fig. 6 represents the resonances with and without antibodies, this type of structure can be used to monitor real-time changes in antibody–protein bonding. However, to achieve this, an acquisition system equipped with a tunable wideband laser and a spectrum analyzer is required to generate and immediately read the data.

There exists a notable distinction between surface and bulk sensitivities. Bulk sensitivity (S_λ) is defined as the spatial shift in resonance position ($\Delta\lambda$) per unit change in bulk refractive index (Δn). It is determined without adlayers on the waveguides [32]. In contrast, surface sensitivity (S), which is more representative of surface-bound proteins or DNA, is defined as the ratio between the resonance shift caused by effective refractive index changes and the refractive index change in the surrounding medium due to concentration variations of the target analyte, also considering the deposited layer thickness [33].

Specifically, for the proposed device, the deposition of anti-IgG, modeled as a 10 nm SiO_2 layer, induces a red resonance shift $\delta\lambda_{\mathrm{RES}}$ of 2.83 nm, as shown in Fig. 6. This results in an effective index change $\Delta n \approx 5.77 \cdot 10^{-3}$, estimated using COMSOL Multiphysics, transitioning from the water surrounding medium in the bare configuration [Fig. 1(b)] to the SiO_2-coated one [Fig. 1(c)], leading to $S_\lambda = 490.49$ nm/RIU. Meanwhile, a surface sensitivity (S) of 21.47 nm/RIU has been calculated, which is comparable to that of plasmonic structures, whose sensitivities are on the order of 30 nm/RIU for a 10 nm layer [34], although it exhibits a larger magnitude than plasmonic biosensors.

Even though plasmonic structures exhibit bulk sensitivities exceeding 1000 nm/RIU [35] and provide very high confinement, they come with significant limitations, including smaller Q factors resulting in larger FWHM, lower resonant amplitude, limiting precise detection, and considerable thermal heating of biomolecules that can lead to sample damage and detection errors due to convection currents and unwanted particle diffusion [36].

Therefore, to assess the goodness of a biosensor, one must consider not only bulk sensitivity but also the Figure of Merit (FOM) for biosensors, which combines the sharpness of the resonance through its FWHM and the biosensor's bulk sensitivity, expressed as FOM $= S_\lambda$/FWHM. Typical FOM values for standard SPR-based sensors range from 75 to 150 RIU^{-1} [37], [38], which are slightly lower than those of standard GMR-based sensors (220–450 RIU^{-1}) [39], [40]. Improvements in FWHM values (less than nm) in PhC cavities result in larger FOM values (525–1550 RIU^{-1}) [40], [41]. The proposed sensor exhibits a FOM ≈ 3892.78 RIU^{-1}, significantly higher than other previously proposed sensors due to its extremely high sensitivity and low FWHM (≈126 pm).

Considering this crucial parameter, it becomes evident that high Q-factor cavity systems are preferable to SPR systems for LOC sensing applications. They can produce easily interpretable signals with substantial transmission spectrum intensity changes. Furthermore, LOC systems demand high reliability, cost-effectiveness, and easily interpretable results, typically employing single-wavelength readout [17]. However, this technique does not match the Lorentzian-shaped resonance devices. For this reason, we have developed a novel box-like device. Even though it possesses lower bulk sensitivity than other biosensors, it boasts a very high FOM and rapid roll-off, enabling cost-effective and error-proof detection, and meeting the requirements of LOC applications.

Table II highlights that our device outperforms the majority of resonant biosensors. However, other competitive devices, as investigated in [9] and [43], exhibit some notable drawbacks. In practical implementations, the deposition of the antibody layer along the tight gaps, characteristic of SWG sensors [9], is challenging due to fabrication limitations. Meanwhile, the device presented in [43] bears some similarities to the one proposed in this work. However, instead

TABLE II

RESONANT BIOSENSOR PERFORMANCE COMPARISON ($*^{EX}$: EXPERIMENTAL RESULTS; $*^{TH}$: THEORETICAL RESULTS)

Topology	Sensor	Sensitivity [nm/RIU]	FOM [RIU^{-1}]	Ref.
GMR	Graphene-tunable GMR sensor$*^{EX}$	291.2	421.4	[39]
	Planar Waveguide Structure$*^{TH}$	6600	224	[40]
PhC Cavities	Porous silicon 1D PhC sensor$*^{TH}$	323	517	[41]
	2D PhC nanocavity$*^{TH}$	400	258.3	[42]
	Defect-mode coupling based PhC sensor$*^{TH}$	810	5028.9	[43]
SWG	SWG$*^{TH}$	605	7,692.3	[9]
	SWG$*^{EX}$	438	1,927.2	[11]
Ring Resonators	WGM ring sensor$*^{EX}$	193	3,112	[44]
	WGM ring sensor$*^{TH}$	361.3	266.43	[8]
Proposed device	Sidewall Grating sensor$*^{TH}$	490.9	3,892.8	-

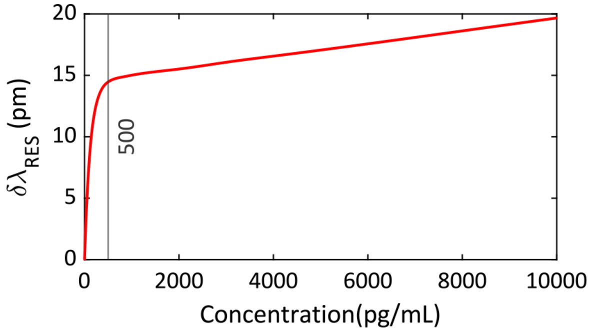

Fig. 7. $\delta\lambda_{RES}$ versus antibody concentration.

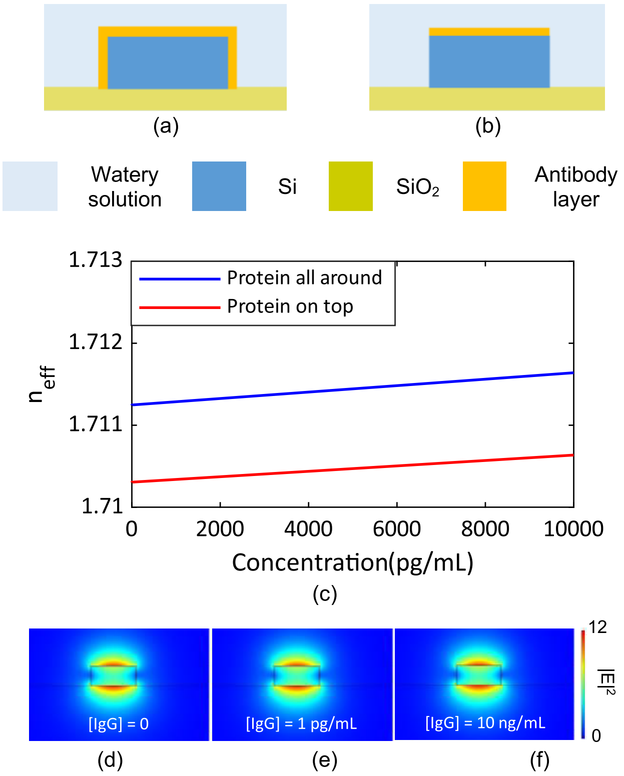

Fig. 8. Cross section of the device with the functionalization layer distribution (a) all around and (b) on the top. (c) Effective refractive index changes of the TM$_0$ mode with the two aforementioned layer distributions by varying the concentration of the target antibody. (d)–(f) Electric field mode distribution for IgG concentration of (d) 0 pg/mL, (e) 1 pg/mL, and (f) 10 ng/mL.

of utilizing coupling cavities created by defects to shape the resonance, they are used to analyze different target analytes. The main issue here is that this structure lacks a central waveguide like ours, making it more susceptible to mechanical stress and, consequently, less suitable for LOC applications.

Furthermore, all the devices under investigation exhibit resolution limits related to Lorentzian shape resonances, which hinders their use in high-sensitivity cost-effective LOC systems.

Further analysis has been carried out to evaluate the impact of the change in protein concentration on the resonance shift and to assess the sensor discernment capability and its dynamic range. The thickness of the antibody–protein layer has been fixed to 10 nm since the protein–antibody bound size is comparable to the free antibody one. According to the experimental results reported in [31], protein concentrations of 1 pg/mL and 1 ng/mL involve an antibody layer refractive index variation of 1×10^{-4} and 1×10^{-3} RIU, respectively. Fig. 7 shows the resonant shift as a function of the protein concentration, starting from the resonance wavelength of the structure with an empty functionalization layer (without bounded proteins). The exponential trend reflects the trend of the effective refractive indices of the grating sub-sections. For concentrations up to 500 pg/mL, $\delta\lambda_{RES}$ varies as 14.46 pm, demonstrating the high-resolved capability of the sensor.

Parametric FEM simulations have been performed through COMSOL Multiphysics to demonstrate the goodness of the chosen functionalization layer distribution. Indeed, the behavior of the proposed device has been analyzed to demonstrate the effective TM refractive index variations by changing the concentration of the target antibody for both the functionalization layer distribution [all around Fig. 8(a) and on the top (b)]. Fig. 8(c) compares the response of the two assumed layer distributions highlighting their similarity and confirming the validity of the aforementioned assumption. However, the distribution of proteins around the whole waveguide is strongly desired to enlarge the surface coverage.

It can be noticed through Fig. 8(d)–(f) that the change in concentration of IgG protein does not significantly affect the field mode distribution but, the effective refractive index change connected to it produces a notable resonance shift, however.

Practical implementations of the biosensor commonly use a single wavelength laser as the source and detect the target analyte concentration change through the measurement of the transmission (reflection) power change [10]. However, a large

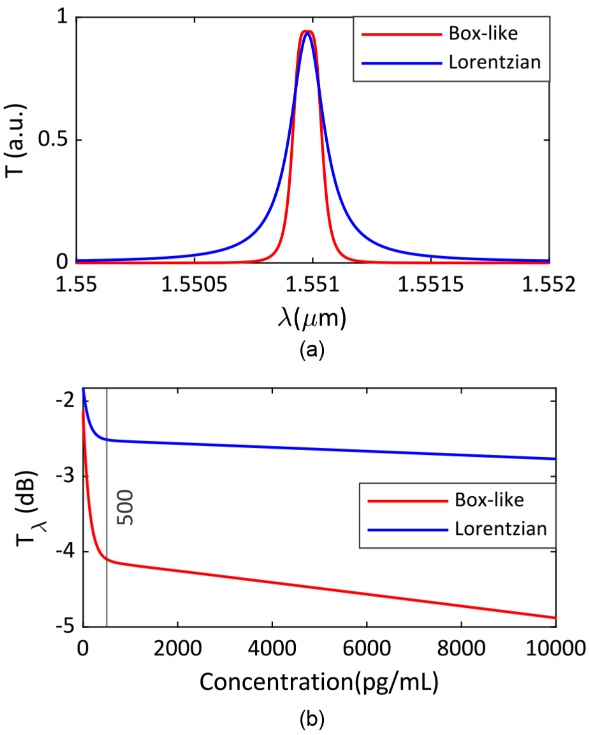

Fig. 9. (a) Transmission spectrum of the sidewall grating with box-like (red curve) and Lorentzian (blue curve) shape. (b) Transmission value T_λ at 1550.92 nm for the sidewall grating with box-like (blue curve) and Lorentzian (red curve) shape versus protein concentration.

resonance shift could collide with the capability of discerning small changes in the transmission power, with a resulting large crosstalk typical of the biosensors with a Lorentzian resonance shape. The large value of $\delta\lambda_{\text{RES}}$ combined with the large roll-off of the proposed biosensor overcomes the aforementioned issues.

To confirm it, a performance comparison between the proposed biosensor with a biosensor characterized by a Lorentzian resonance shape with similar Q-factors and sensitivity S_λ has been carried out. To achieve a resonance Lorentzian shape with a Q-factor of 10^4, a sidewall grating, based on the same technology discussed in Section II, has been designed with $N_t = 64$, $N_{\text{def}} = 1$, and $m = 100$, with resulting Q-factor $\approx 8.9 \times 10^3$ and ER $\approx$ 16 dB.

The slight mismatch between the FWHMs of the two resonances (=40 pm) cannot be overcome, since it depends on the number of defects (N_{def}), the number of sections (N_t), and the grating order (m), which cannot be continuously tuned to perfectly match the desired mismatch [25]. However, since the detection approach involves measuring the amplitude changes, related to the variation of the protein concentration, at a fixed wavelength, that will be designed as the crossing point between the two shapes, where the amplitude is the same, the mismatch between FWHMs is negligible.

As arises from the resonance comparison in Fig. 9(a), the Lorentzian-shaped peak shows a roll-off about two times lower than the box-like one (from −10.50 to 5.85 dB/oct.), which corresponds to the concentration discerning capability.

In fact, by setting the operation wavelength at the center of the left resonance edge (=1550.92 nm), a sharp transmission change from ≈ -2.1 to -4.2 dB has been calculated up to 500 pg/mL [slope of $3.83 \cdot 10^{-3}$ dB/(pg/mL)] for the box-like biosensor, larger with respect to the transmission change related to the Lorentzian-shape (−1.8 to −2.2 dB), and a slope of $1.37 \cdot 10^{-3}$ dB/(pg/mL), with a resulting much larger capability of discerning small concentrations of proteins [see Fig. 9(b)]. Moreover, from a practical point of view, the wide transmission change of the proposed sensors makes it less sensitive to noise with respect to Lorentzian-shape sensor, due to larger noise margins, improving the accuracy of sensing.

As revealed by the analysis conducted, the proposed device can be effectively utilized by harnessing both the wavelength shift and the fast roll-off modes. However, the wavelength shift mode requires a high-resolution spectrum analyzer to detect small variations in the resonance frequency, whereas the roll-off mode performs significantly better. This is attributed to the inherent characteristics of the resonance shape itself, which allows for the detection of small changes in the concentration of the target analyte using a standard photodetector. This approach leads to cost savings and a more compact device.

From a practical point of view, the fabrication of the proposed device could be carried out by advanced lithographic methods such as electron-beam lithography (EBL). Considering manufacturing tolerances of approximately ±10 nm, a FWHM = 197.76 pm has been achieved, 1.7 times larger than the designed case, although with a larger roll-off = 13.40 dB/oct. The FWHM variation leads to a decrease of transmission sensitivity with respect to the protein concentration [=to a decrease in the ratio between power variation and transmission (=$2.53 \cdot 10^{-3}$ dB/(pg/mL)], albeit still higher than the Lorentzian case.

After the fabrication, a well-defined biofunctionalization protocol specific to sensor and target biomolecules could be developed. In this regard, a proper biofunctionalization of the sensor surface and reliable immobilization of bioreceptors over the detection area is the most crucial step for achieving high detection performance label-free biosensors and therefore deserves careful consideration and observations.

The biofunctionalization process involves chemical modification of the sensor substrate to provide a homogeneous layer that spans the sensing area by presenting terminal functional groups capable of binding receptors.

In the framework of the proposed Si-based biosensor, the chemical modification of the surface is carried out by salinization [47]. Such a process employs organofunctional silanes, to establish a chemical connection between inorganic, silicon-containing surfaces, and organic compounds.

The most common protocols employ amino-functional silanes, such as 3-Aminopropyl(diethoxy) methyl silane (APDEMS) or the (3-aminopropyl) triethoxysilane (APTES), which provide stable films on the sensor surface [45], [46], [47].

Once the functional chemical scaffold is formed on the sensor surface, the next step is the anchoring points for bioreceptors to capture their target molecules; the compound generally used to obtain a very stable and robust bioreceptor is glutaraldehyde (CH2)3(CHO)2 [35]. The biofunctionalization process ends with incubating antibodies and antigens and appropriately washing them with PBS.

To immobilize molecules on the chemically modified sensor surfaces effectively and to preserve molecules bioactivity enabling selective capture of the target antigen, the functionalization process should be carried out overall by the sensor. In this way, the molecule bioactivity will be preserved, and highly selective molecular bonds could occur.

IV. CONCLUSION

A novel ultra-compact SOI biosensor with a Q-factor of about 1.2×10^4 and an ER of 15.35 dB has been designed for single-wavelength interrogation systems. The Newtonian distribution of the defects along the whole grating path provides a box-like shaped resonance at about 1550 nm. As a protein biosensor, the proposed device combines a very high sensitivity ($=490.49$ nm/RIU) with a very large roll-off ($=-10.50$ dB/oct.), about five times larger than a Lorentzian shape with a similar Q-factor. A concentration of 500 pg/mL leads to a transmission change of more than 4 dB, making it easy to distinguish similar values of concentrations, and also avoiding crosstalk issues typically related to Lorentzian resonances. The reported performance represents a clear improvement with respect to the state-of-the-art, with the highest FOM ($\approx$3892.78 RIU^{-1}) reported so far, according to our knowledge, making the proposed sensor suitable as a biosensor to support the predictive medicine counteract the spread of cancer issues.

REFERENCES

[1] L. Jiang et al., “A quantitative proteome map of the human body,” *Cell*, vol. 183, no. 1, pp. 269–283, 2020.

[2] J. Juan-Colás, S. Johnson, and T. Krauss, “Dual-mode electro-optical techniques for biosensing applications: A review,” *Sensors*, vol. 17, no. 9, p. 2047, Sep. 2017.

[3] L. Torrijos-Morán, B. D. Lisboa, M. Soler, L. M. Lechuga, and J. García-Rupérez, “Integrated optical bimodal waveguide biosensors: Principles and applications,” *Results Opt.*, vol. 9, Dec. 2022, Art. no. 100285.

[4] D. Duval and L. M. Lechuga, “Breakthroughs in photonics 2012: 2012 breakthroughs in lab-on-a-chip and optical biosensors,” *IEEE Photon. J.*, vol. 5, no. 2, Apr. 2013, Art. no. 0700906.

[5] J. Sabek et al., “Experimental study of an evanescent-field biosensor based on 1D photonic bandgap structures,” *Beilstein J. Nanotechnol.*, vol. 10, pp. 967–974, Apr. 2019.

[6] D. Duval and L. M. Lechuga, “Optical waveguide biosensors,” in *Photonics: Biomedical Photonics, Spectroscopy, and Microscopy*. Hoboken, NJ, USA: Wiley, 2015, ch. 8.

[7] P. Kumaar and A. Sivasubramanian, “Optimization of the transverse electric photonic strip waveguide biosensor for detecting diabetes mellitus from bulk sensitivity,” *J. Healthcare Eng.*, vol. 2021, pp. 1–8, Nov. 2021.

[8] A. K. Ajad, M. J. Islam, M. R. Kaysir, and J. Atai, “Highly sensitive bio sensor based on WGM ring resonator for hemoglobin detection in blood samples,” *Optik*, vol. 226, Jan. 2021, Art. no. 166009.

[9] R. Singh, V. Priye, and D. Chack, “Highly sensitive refractive index-based sensor for DNA hybridization using subwavelength grating waveguide,” *IETE Tech. Rev.*, vol. 39, no. 6, pp. 1463–1472, Nov. 2022.

[10] L. Chrostowski et al., “A silicon photonic evanescent-field sensor architecture using a fixed-wavelength laser,” in *Proc. SPIE*, vol. 11692, pp. 115–129, Mar. 2021.

[11] L. S. Puumala et al., “An optimization framework for silicon photonic evanescent-field biosensors using sub-wavelength gratings,” *Biosensors*, vol. 12, no. 10, p. 840, Oct. 2022.

[12] L. Torrijos-Moran, A. Griol, and J. García-Rupérez, “Bimodal waveguide sensors enabled by subwavelength grating structures,” in *Proc. Integr. Photonics Res., Silicon Nanophotonics Conf. (IPRSN)*, 2020, pp. ITu4A-4.

[13] E. Luan, H. Shoman, D. Ratner, K. Cheung, and L. Chrostowski, “Silicon photonic biosensors using label-free detection,” *Sensors*, vol. 18, no. 10, p. 3519, Oct. 2018.

[14] J. García-Rupérez and L. Torrijos-Morán, “Bimodal interferometric photonic sensors based on periodic configurations,” in *Proc. Opt. Sensors Conf.*, 2021, pp. SF2D-1.

[15] G. J. Triggs, Y. Wang, C. P. Reardon, M. Fischer, G. J. O. Evans, and T. F. Krauss, “Chirped guided-mode resonance biosensor,” *Optica*, vol. 4, no. 2, p. 229, Feb. 2017.

[16] I. Barth, D. Conteduca, C. Reardon, S. Johnson, and T. F. Krauss, “Common-path interferometric label-free protein sensing with resonant dielectric nanostructures,” *Light, Sci. Appl.*, vol. 9, no. 1, p. 96, Jun. 2020.

[17] S. J. Ward, R. Layouni, S. Arshavsky-Graham, E. Segal, and S. M. Weiss, “Morlet wavelet filtering and phase analysis to reduce the limit of detection for thin film optical biosensors,” *ACS Sensors*, vol. 6, no. 8, pp. 2967–2978, Aug. 2021.

[18] D. Conteduca, I. Barth, G. Pitruzzello, C. P. Reardon, E. R. Martins, and T. F. Krauss, “Dielectric nanohole array metasurface for high-resolution near-field sensing and imaging,” *Nature Commun.*, vol. 12, no. 1, pp. 1–9, Jun. 2021.

[19] T. Horikawa, D. Shimura, and T. Mogami, “Low-loss silicon wire waveguides for optical integrated circuits,” *MRS Commun.*, vol. 6, no. 1, pp. 9–15, Mar. 2016.

[20] C. A. Barrios et al., “Label-free optical biosensing with slot-waveguides,” *Opt. Lett.*, vol. 33, no. 7, pp. 708–710, 2008.

[21] C. A. Barrios, “Analysis and modeling of a silicon nitride slot-waveguide microring resonator biochemical sensor,” *Opt. Sensors*, vol. 7356, pp. 60–69, May 2009.

[22] H.-K. Na, J.-S. Wi, H. Y. Son, J. G. Ok, Y.-M. Huh, and T. G. Lee, “Discrimination of single nucleotide mismatches using a scalable, flexible, and transparent three-dimensional nanostructure-based plasmonic miRNA sensor with high sensitivity,” *Biosensors Bioelectron.*, vol. 113, pp. 39–45, Aug. 2018.

[23] H. Zhang et al., “Design and fabrication of silicon nanowire-based biosensors with integration of critical factors: Toward ultrasensitive specific detection of biomolecules,” *ACS Appl. Mater. Interfaces*, vol. 12, no. 46, pp. 51808–51819, Nov. 2020.

[24] X. Wang, “Silicon photonic waveguide Bragg gratings,” Ph.D. dissertation, Faculty Appl. Sci., Dept. Elect. Comput. Eng., Univ. British Columbia, Vancouver, BC, Canada, 2013.

[25] G. Brunetti, F. Dell’Olio, D. Conteduca, M. N. Armenise, and C. Ciminelli, “Ultra-compact tuneable notch filter using silicon photonic crystal ring resonator,” *J. Lightw. Technol.*, vol. 37, no. 13, pp. 2970–2980, Jul. 2019.

[26] R. M. Knox and P. P. Toulios, “Integrated circuits for the millimeter through optical frequency range,” in *Proc. Symp. Submillimeter Waves*, vol. 20, May 1970, pp. 497–515.

[27] M. Born and E. Wolf, *Principles of Optics: Electromagnetic Theory of Propagation, Interference and Diffraction of Light*. Amsterdam, The Netherlands: Elsevier, 2013.

[28] R. Halir et al., “Colorless directional coupler with dispersion engineered sub-wavelength structure,” *Opt. Exp.*, vol. 20, no. 12, pp. 13470–13477, 2012.

[29] G. Brunetti, G. Marocco, A. Di Benedetto, A. Giorgio, M. N. Armenise, and C. Ciminelli, “Design of a large bandwidth 2×2 interferometric switching cell based on a sub-wavelength grating,” *J. Opt.*, vol. 23, no. 8, 2021, Art. no. 085891.

[30] C. Lee, S. Jeon, S. J. Kim, and S. J. Kim, “Near-flat top bandpass filter based on non-local resonance in a dielectric metasurface,” *Opt. Exp.*, vol. 31, no. 3, pp. 4920–4931, 2023.

[31] G. Hernàndez, “Fabry–Perot interferometers,” Ph.D. dissertation, Cambridge Univ. Press, Cambridge, U.K., 1988.

[32] P. Berini, “Bulk and surface sensitivities of surface plasmon waveguides,” *New J. Phys.*, vol. 10, no. 10, Oct. 2008, Art. no. 105010.

[33] J. Homola, “Surface plasmon resonance sensors for detection of chemical and biological species,” *Chem. Rev.*, vol. 108, no. 2, pp. 462–493, Feb. 2008.

[34] A. E. Cetin, D. Etezadi, B. C. Galarreta, M. P. Busson, Y. Eksioglu, and H. Altug, “Plasmonic nanohole arrays on a robust hybrid substrate for highly sensitive label-free biosensing,” *ACS Photon.*, vol. 2, no. 8, pp. 1167–1174, Aug. 2015.

[35] C. M. Dundas, D. Demonte, and S. Park, “Streptavidin-biotin technology: Improvements and innovations in chemical and biological applications,” *Appl. Microbiol. Biotechnol.*, vol. 97, no. 21, pp. 9343–9353, Nov. 2013.

[36] D. Conteduca et al., “Exploring the limit of multiplexed near-field optical trapping,” *ACS Photon.*, vol. 8, no. 7, pp. 2060–2066, Jul. 2021.

[37] Y. E. Monfared, “Refractive index sensor based on surface plasmon resonance excitation in a D-shaped photonic crystal fiber coated by titanium nitride,” *Plasmonics*, vol. 15, no. 2, pp. 535–542, Apr. 2020.

[38] M. Maleki and M. Mehran, “Analytical investigation and systematic design approach for high-sensitivity guided mode resonance sensors with graphene-enabled tunability,” *IEEE Sensors J.*, vol. 22, no. 14, pp. 14177–14184, Jul. 2022.

[39] P. Urbancova, J. Chylek, P. Hlubina, and D. Pudis, “Guided-mode resonance-based relative humidity sensing employing a planar waveguide structure,” *Sensors*, vol. 20, no. 23, p. 6788, Nov. 2020.

[40] A. K. Goyal, “Design analysis of one-dimensional photonic crystal based structure for hemoglobin concentration measurement,” *Prog. Electromagn. Res. M*, vol. 97, pp. 77–86, 2020.

[41] M. H. Sani, A. Ghanbari, and H. Saghaei, “High-sensitivity biosensor for simultaneous detection of cancer and diabetes using photonic crystal microstructure,” *Opt. Quantum Electron.*, vol. 54, no. 1, pp. 1–14, Jan. 2022.

[42] X. Qing and M. H. Sani, “Optical refractive index sensor for detection of N_2, He and CO_2 gases based on square resonance nanocavity in 2D photonic crystal,” *Opt. Commun.*, vol. 490, Jul. 2021, Art. no. 126940.

[43] C. Wu, X. Liu, S. Feng, X. Chen, C. Li, and Y. Wang, “High-sensitivity silicon-based photonic crystal refractive index biosensor based on defect-mode coupling,” *Opt. Commun.*, vol. 427, pp. 409–417, Nov. 2018.

[44] R. Guider et al., “Sensitivity and limit of detection of biosensors based on ring resonators,” *Sens. Bio-Sens. Res.*, vol. 6, pp. 99–102, Dec. 2015.

[45] F. Zhang et al., “Chemical vapor deposition of three aminosilanes on silicon dioxide: Surface characterization, stability, effects of silane concentration, and cyanine dye adsorption,” *Langmuir*, vol. 26, no. 18, pp. 14648–14654, Sep. 2010.

[46] J. H. Moon, J. W. Shin, S. Y. Kim, and J. W. Park, “Formation of uniform aminosilane thin layers: An imine formation to measure relative surface density of the amine group,” *Langmuir*, vol. 12, no. 20, pp. 4621–4624, Jan. 1996.

[47] S. Kumar, I. Haq, J. Prakash, and A. Raj, “Improved enzyme properties upon glutaraldehyde cross-linking of alginate entrapped xylanase from *Bacillus licheniformis*,” *Int. J. Biol. Macromolecules*, vol. 98, pp. 24–33, May 2017.

Annarita di Toma received the M.Sc. (cum laude) degree in electronic engineering from Politecnico di Bari, Bari, Italy, in 2022. She is currently pursuing the Ph.D. degree for the development of photonic devices and systems mainly in the context of biomedical and Space field.

In 2022, she has joined the Optoelectronics Group, Bari.

Giuseppe Brunetti received the M.Sc. (cum laude) degree in electronic engineering and the Ph.D. degree in information engineering from the Politecnico di Bari, Bari, Italy, in 2016 and 2020, respectively. His Ph.D. activity was focused on innovative photonic and optoelectronic devices for the Space applications with European Space Agency (ESA) sponsorship.

Since December 2020, he has been an Assistant Professor of Electronics at the Politecnico di Bari with a grant entitled “Electronic Systems for Rapid Analysis of Antimicrobial Susceptibility.” His research interests include integrated optoelectronics and photonics devices and systems mainly in the biomedical and space field context.

Paola Colapietro received the M.Sc. (cum laude) degree in electronic engineering from the Politecnico di Bari, Bari, Italy, in 2022, where she is currently pursuing the Ph.D. (program Industry 4.0) at the Politecnico di Bari. The Ph.D activity aims to the development of photonic devices and systems in the context of biomedical field.

In 2022, she has joined the Optoelectronics Group.

Caterina Ciminelli (Senior Member, IEEE) received the Laurea and Ph.D. degrees in electronic engineering from the Politecnico di Bari, Italy, in 1996 and 2000, respectively.

From 1999 to 2002, she did industrial research activity on optoelectronic components and subsystems with the Research and Development Division of Pirelli Optical Systems and Cisco Photonics, Italy, before joining the Politecnico di Bari, as an Assistant Professor of Electronics in 2002. From 2012 to 2021, she has been an Associate Professor. Since 2021, she has been a Full Professor with the Politecnico di Bari where she is the scientist responsible for the Optoelectronics Laboratory. Her research interests include integrated optoelectronics and photonics.

Open Access funding provided by ‘Politecnico di Bari’ within the CRUI-CARE Agreement